I&EC research
Industrial & Engineering Chemistry Research

pubs.acs.org/IECR

Article

Understanding Potential Losses and pH Distribution in the Electrochemical Nitrate Reduction Reaction to Ammonia

Maryam Ahmadi and Mohammadreza Nazemi*

Cite This: *Ind. Eng. Chem. Res.* 2024, 63, 9315−9328

Read Online

ACCESS | Metrics & More | Article Recommendations | Supporting Information

ABSTRACT: Electrochemical nitrate reduction reaction (NO_3^-RR) to ammonia is a promising route to eliminate one of the major pollutants in surface water and groundwater. When powered by renewable electricity, electrolysis provides a sustainable method to generate ammonia from nitrate ions, facilitating the transition from a linear to a circular economy. Optimizing the physical and chemical properties of electrolysis cells is crucial to making this process economically viable for widespread implementation. Here, we explore how the choice of current density, conductivity, pH, interelectrode distance, membrane, catalyst, and buffer solution affect nitrate removal performance and efficiency. We developed a modeling framework to investigate the cell characteristics and fluid dynamics during electrochemical NO_3^-RR using both laminar and bubbly flows. To obtain more precise results, we employed the bubbly flow model (i.e., multiphase fluid) to take into account how gas production near the electrode surface affects liquid velocity, pH distribution, and, ultimately, potential losses. We exploit mass transfer theory to include the current density effect on migration and diffusion. In the absence of a buffer solution, the Nernstian loss became a significant portion of the polarization loss, which increased with current density. We identified the positive effect of the membrane on energy efficiency as being more significant at smaller interelectrode distances. This study provides insights into the origin of potential losses and pH distribution, enabling electrochemical cell optimization for renewable fuel synthesis.

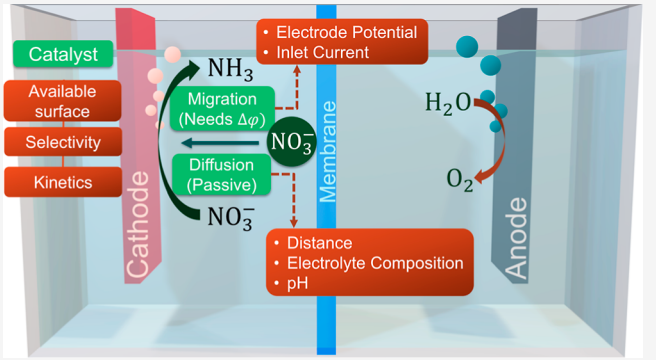

INTRODUCTION

The nitrogen cycle, crucial for sustaining all life forms, involves natural dinitrogen (N_2) fixation through the enzyme nitrogenase, but this process has been insufficient to meet growing global needs.[1] This necessitates artificial N_2 fixation into various nitrogen-based compounds, such as ammonia (NH_3), nitric acid (HNO_3), and hydrazine (N_2H_4), to meet diverse demands across a wide variety of sectors, including agriculture and chemical industries.[2−4] Wastewater resources, integral to the nitrogen cycle, often contain high levels of nitrate (NO_3^-), requiring treatment from various sources, such as industrial, municipal, and agricultural wastewater. Although nitrate is beneficial for plant growth, in excess amounts, it accelerates eutrophication, causes dramatic algae growth, and alters aquatic ecosystems. Furthermore, nitrate, even at low concentrations (>10 mg/L), contaminates surface and groundwater, resulting in serious health issues such as blue baby syndrome and liver damage.[5,6] Catalytic denitrification, particularly through electrocatalysis, represents a carbon-free solution powered by renewable energy sources, offering potential benefits in reducing nitrate concentrations in waste streams. Improvements in catalyst selectivity, durability, and activity toward desired products could contribute to the widespread deployment of this technology.[7,8] One of the desired products of electrochemical nitrate reduction reaction (NO_3^-RR) is ammonia due to its wide range of applications in industry, agriculture, and chemical manufacturing.[9−11] The increasing global trend in the ammonia market, with an approximate compound annual growth rate (CAGR) of 5.1%, underscores the growing interest in this commodity chemical.[12]

Several recent experimental studies have focused on electrochemical NO_3^-RR to benchmark catalyst selectivity, faradaic efficiency, and system maximum current densities.[13−26] Computational studies can provide a tool to minimize potential losses. Further, they are versatile platforms for experimentalists to optimize electrochemical operating conditions. In electrochemical computational studies, the mass transfer theory includes the effects of migration, diffusion, and convection. In prior studies, mass transport models were used

Received: December 21, 2023
Revised: February 17, 2024
Accepted: March 12, 2024
Published: March 26, 2024

https://doi.org/10.1021/acs.iecr.3c04540
Ind. Eng. Chem. Res. 2024, 63, 9315−9328

to simulate fuel cell current density distribution[27] and species concentration profiles.[28] Spatiotemporal concentration profiles near electrode surfaces were investigated to examine pH distribution in water-splitting cells.[29−31] These studies are not only important for material selection and informing design criteria but also play an important role in calculating polarization loss. Polarization loss studies exist for systems such as carbon dioxide[32] and water electrolysis cells.[33] To the best of our knowledge, there are currently no studies that perform a similar analysis for the NO_3^-RR to pinpoint the various origins of potential losses, which would be key to finding effective methods of minimizing polarization loss in solutions containing NO_3^- ions.

Here, we aim to establish a comprehensive computational framework for NO_3^-RR to ammonia using the electrochemical and transport properties of cells. In these studies, we employed 1D and 2D models to examine spatiotemporal concentration profiles and pH distributions near the electrode surfaces and in the bulk solution. We considered a wide range of current densities (0−500 mA/cm^2) and separated cathodic and anodic reactions according to eqs 1, 2 and S1−S8 for acidic and alkaline media at T = 25 °C.[34]

$$NO_3^- + 10H^+ + 8e^- \rightarrow 3H_2O + NH_4^+ \quad (1)$$

$$NO_3^- + 6H_2O + 8e^- \rightarrow 9OH^- + NH_3 \quad (2)$$

We studied both bubbly and laminar flow fluid dynamics models to determine the role of ammonia and oxygen gas production near electrode surfaces on the liquid velocity and pH distribution of the cell. This modeling platform will assist in future industrial reactor design and material selection. In addition, it will help to pinpoint the optimum operating conditions of the system, including current density, pH, and conductivity. This ultimately results in the design of a fit-for-purpose electrolyzer for chemical manufacturing and wastewater treatment.

THEORY

Polarization Loss Theory. Ohmic loss, diffusion loss, and Nernstian loss are categorized as mass transfer potential loss or polarization loss. The electrolyte resists the movement of ions based on its ionic conductivity, which results in potential loss. We determined this loss using eq 3

$$\Delta\phi_{\text{Ohmic}} = iR \quad (3)$$

where i (A) is the input current, and R (Ω) is the electrolyte ionic resistance, which is given by eq 4.

$$R = \frac{L}{\kappa A} \quad (4)$$

Where κ (S/m) is the solution conductivity, L (m) is the cell length, and A (m^2) is the cell cross-sectional area. The solution conductivity is experimentally measured, and raw data is available for different salt concentrations of aqueous solutions at T = 25 °C.[35] Here, we mainly focus on near-neutral pH, and potassium nitrate (KNO_3) is the major salt in the solution, with a concentration of 0.5 M or 5% wt. To determine potential loss, we compared solutions with different pH and salt concentrations and presented their conductivities in Table S1.

By combining eqs 3 and 4 and considering changes in conductivity along the cell, we can rewrite the Ohmic loss formula in a new form as eq 5.

$$\Delta\phi_{\text{Ohmic}} = \int_0^L \frac{i_l}{\kappa}\,dx \quad (5)$$

where i_l (A/m^2) is the electrolyte current density. The cathode surface position is at x = 0 m, and the anode surface position is at $x = L$ m. We employed eq S9 to model the conductivity gradient along the cell and over time.[36] As a result of the ionic concentration gradient at electrode surfaces and along the cell, species diffuse and react at the electrode surface under the applied bias. We calculated this potential loss using eq 6

$$\Delta\phi_{\text{diffusion}} = \sum_i \int_0^L \frac{Fz_iD_i\nabla c_i}{\kappa}\,dx \quad (6)$$

where c_i (mol/m^3) is the species i concentration, D_i (m^2/s) is the diffusion coefficient, z_i is the charge number, and F (96,485 C/mol) is the Faraday's constant. We listed diffusion coefficients and bulk concentrations of species in Table S2.[37] The combination of diffusion loss and Ohmic loss is termed solution loss. We used the Nernst equation for the half-cell reaction to derive the Nernstian loss (eq 7)

$$E = E^0 - \frac{RT}{nF}\ln Q \quad (7)$$

where R (8.314 J/mol K) is the gas constant, T (293.15 K) is the temperature, Q is the reaction quotient, and E^0 (V) is the reaction formal potential. As reactants are consumed and the products are produced at the electrode surface, the quotient increases, resulting in a higher potential. This increase in potential represents the Nernstian loss. We calculated the Nernstian loss based on cathodic and anodic reactions with reacting ions, including nitrates, hydroxides, and protons (eq 8)[38]

$$\begin{aligned}\Delta\phi_{\text{Nernstian}} = {} & 2.303\frac{RT}{F}(\text{pH}_{\text{cathode}} - \text{pH}_{\text{Bulk}}) \\ & + 2.303\frac{RT}{F}(\text{pH}_{\text{Bulk}} - \text{pH}_{\text{anode}}) \\ & + \frac{RT}{F}\ln\left(\frac{c_{NO_3^-,\text{Bulk}}}{c_{NO_3^-,\text{cathode}}}\right)\end{aligned} \quad (8)$$

Mass Transfer Theory. We modeled concentration profiles along the cell and over time using mass transfer theory to calculate the polarization loss. The Nernst−Plank equation defines total molar flux, which leads to the calculation of the concentration profiles (eq 9)[39]

$$\begin{aligned}N_i = {} & \left(-D_i\frac{\partial c_i}{\partial x}\right)_{\text{diffusion}} - \left(z_iu_iFc_i\frac{\partial\Phi_1}{\partial x}\right)_{\text{migration}} \\ & + (c_iv(x))_{\text{convection}}\end{aligned} \quad (9)$$

where N_i (mol/m^2 s) is the total molar flux, Φ_1 (V) is the electrolyte potential, $v(x)$ (m/s) is the convection velocity, and u_i (m^2/V s) is the ion mobility. We used eq 10 to calculate the ion mobility

$$u_i = \frac{D_i}{RT} \quad (10)$$

Input current density is the sum of the ionic flux in electrolysis cells (eq 11).

https://doi.org/10.1021/acs.iecr.3c04540
Ind. Eng. Chem. Res. 2024, 63, 9315−9328

$$i_l = F \sum_i z_i N_i \tag{11}$$

Electroneutrality, or charge conversion, is an inherent characteristic of electrochemical systems, which is described in eq 12. We considered the K^+ cation as an inert species to satisfy charge conservation.

$$\sum_i z_i c_i = 0 \tag{12}$$

Transport of species in electrolytes and membranes must satisfy the mass conservation law (eq 13)

$$\frac{\partial c_i}{\partial t} + \frac{\partial N_i}{\partial x} = R_i \tag{13}$$

where R_i (mol/m^3 s) is the reaction rate. We can measure the reaction rate for nonredox reactions based on forward and backward reaction rates. For the water equilibrium reaction (eq 14), the forward reaction rate ($K_{W,f}$) is 2.4 × 10^{-5} and the equilibrium constant (K_W) is 10^{-4}; thus, we can write the reaction rates using eqs 15 and 16 for protons and hydroxide ions in the bulk

$$H_2O \rightarrow H^+ + OH^- \tag{14}$$

$$\frac{\partial c_{H^+}}{\partial t} + \frac{\partial N_{H^+}}{\partial x} = K_{W,f} - \frac{K_{W,f}}{K_W} c_{H^+} c_{OH^-} \tag{15}$$

$$\frac{\partial c_{OH^-}}{\partial t} + \frac{\partial N_{OH^-}}{\partial x} = K_{W,f} - \frac{K_{W,f}}{K_W} c_{H^+} c_{OH^-} \tag{16}$$

The water equilibrium reaction is the only reaction happening in bulk in the absence of the buffer solution.[40] In the boundary layers near the electrodes, both hydroxide ions and protons are involved in the electrode surface reactions. Thus, we should consider the reaction rate resulting from the local current density in addition to the equilibrium reaction. This rate is added to the right-hand side of the eqs 15 and 16. We used dipotassium phosphate and monopotassium phosphate for the buffer solution. We listed their basic and acidic constants in Table S3 and included their equilibrium reactions in eqs S10−S15. We modeled the electrode current density vector according to eq 17.

$$i_s = -\sigma_s \nabla \phi_s \tag{17}$$

where ϕ_s (V) is the electrode potential and σ_s (S/m) is the electrode conductivity. We modeled the anode as ruthenium oxide (RuO_2)[41] with a conductivity equal to 2.8 × 10^4 S/m[42] and the cathode as ruthenium cobalt alloy ($Ru_{15}CO_{85}$)[43] with a conductivity equal to 1.7 × 10^7 S/m.

To satisfy charge conservation, current densities remain constant with respect to the position (eqs 18 and 19).

$$\frac{\partial i_l}{\partial x} = 0 \tag{18}$$

$$\frac{\partial i_s}{\partial x} = 0 \tag{19}$$

The anode has a constant input current density with an initial boundary electric potential value of 2 V, and the cathode has an electric potential value of −1 V.

Electrode Surface Reactions and Kinetics Theory. We modeled the electrode reaction rate for each species involved in the electrode surface reactions using eq 20

$$R_i = \frac{-\nu_i i_{loc}}{nF} \tag{20}$$

where i_{loc} (A/m^2) is the electrode local current density, and ν_i is the stoichiometric coefficient of the species. We used the Butler−Volmer equation to model the electrode local current density (eq 21).

$$i_{loc} = i_0 \left(\exp\left(\frac{\alpha_a F \eta}{RT} \right) - \exp\left(\frac{\alpha_c F \eta}{RT} \right) \right) \tag{21}$$

where η (V) is the overpotential, α is the symmetry factor for the cathode and anode reactions, and i_0 (A/m^2) is the exchange current density. We then employed the law of mass action to determine the exchange current density using eq 22. This law demonstrates the correlation between current density and surface concentrations of reactants and products.[44]

$$i_0 = i_{0,ref}(T) \prod_{i,\nu_i>0} \left(\frac{c_i}{c_{i,ref}} \right)^{\alpha_c \nu_i / n} \prod_{i,\nu_i<0} \left(\frac{c_i}{c_{i,ref}} \right)^{-\alpha_a \nu_i / n} \tag{22}$$

where $i_{0,ref}$ (A/m^2) is the catalyst exchange current density at T = 298.15 K. For the OER reaction at the anode, α_a = 0.62, α_c = 0.38, and $i_{0,ref}$ = 1.12 × 10^{-5} A/cm^2.[41] For NO_3^-RR, α_a = 0.88, α_c = 0.12, and $i_{0,ref}$ = 2.24 × 10^{-5} A/cm^2.[43] To model equilibrium potentials for the cathode and anode, we used the Nernst equation.

Ion Exchange Membrane Theory. We modeled the membrane as a cation exchange membrane (CEM) with a thickness of 100 μm located at the center of the cell. The membrane has a space charge equal to −1 C/m^3 and an electrolyte volume fraction (ϵ) equal to 0.5. We reduced diffusion coefficients by multiplying them by 0.1 for positive ions and 0.01 for negative ions. The mass conservation equation is modified by considering the electrolyte volume fraction (eq 23).

$$\frac{\partial c_i}{\partial t} + \frac{\partial N_i}{\partial x} = \epsilon R_i \tag{23}$$

The potential distribution in the membrane is calculated by eq 24, where ϕ_l is the electrolyte potential, ϕ_m is the membrane potential, $c_{i,m}$ is the species concentration across the membrane, and $c_{i,l}$ is the species concentration in the electrolyte.

$$\phi_l - \phi_m = -\frac{RT}{z_i T} \ln \frac{c_{i,l}}{c_{i,m}} \tag{24}$$

Charge conservation along the membrane is given by eq 25, where ρ_{fix} (C/m^3) is the membrane fixed space charge.

$$\rho_{fix} + \sum_i z_i c_i = 0 \tag{25}$$

Pourbaix Diagram Theory. The Pourbaix diagram shows the thermodynamic stability of the species at the given pH, potential, and temperature. Hydrogen evolution reaction (HER) is the primary cathodic competing reaction with NO_3^-RR. Oxygen evolution reaction (OER) happens at the anode surface. Both the cathodic and anodic reaction potentials are pH-dependent (Figures 1 and S1). We assumed 100% Faradaic efficiency toward ammonia production. In reality, this can be accomplished by engineering catalysts and electrolytes that suppress HER effectively.[24,45,46] The distribution of ammonium and ammonia is dependent on the solution

https://doi.org/10.1021/acs.iecr.3c04540
Ind. Eng. Chem. Res. 2024, 63, 9315−9328

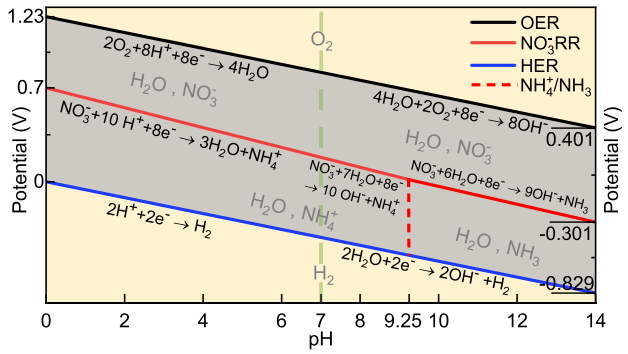

Figure 1. Pourbaix diagram for the anodic reaction (OER) and cathodic competing reactions (NO_3^-RR and HER) at T = 298.15 K. The diagram also shows the transition from NH_4^+ to NH_3 at pK_a of 9.251.

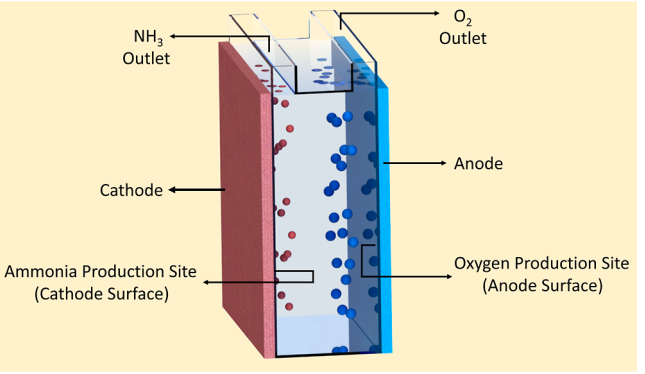

Figure 2. 2D Model domain with boundaries corresponding to the anode, cathode, NH_3 production site, O_2 production site, and their outlets.

pH and temperature. The acid−base reaction between ammonium and ammonia happens at the acid dissociation constant, pK_a = 9.251, which was calculated using eq 26 at T = 298.15 K, indicating the dependency of the ammonia dissociation constant on the temperature.

$$\mathrm{p}K_a = 0.0901821 + 2729.92/T\ (\mathrm{K}) \tag{26}$$

$$f_{\mathrm{NH_3}} = \frac{1}{10^{9.251-\mathrm{pH}} + 1} \tag{27}$$

Laminar Flow Theory. We simulated 1D and 2D models using laminar flow physics and considered the electrode width equal to 2 mm, the electrode surface area equal to 25 cm^2, two different cell lengths equal to 6 mm and 2 cm, and the membrane length equal to 100 μm (Figures S2 and S3). eqs 28 and 29 are the momentum and continuity equations for modeling laminar flow physics.

$$\rho\frac{\partial u}{\partial t} + \rho u\cdot\nabla u = -\nabla p + \nabla\cdot[\mu(\nabla u + \nabla u^{\mathrm{T}})] + \rho g + F \tag{28}$$

$$\rho\nabla\cdot u = 0 \tag{29}$$

where p (Pa) is the pressure, ρ (kg/m^3) is the density, g (m/s^2) is the gravity vector, F (N/m^3) is any additional volume force, u (m/s) is the liquid velocity, and μ (Pa s) is the liquid viscosity.

Bubbly Flow Theory. We assumed two gas production sites at the cathode and anode surfaces. Produced gas bubbles have a small volume fraction, and their velocity can be modeled by the slip model (Figure 2). Therefore, solving fluid mechanics physics is possible by solving one Navier−Stocks equation. The momentum equation for this combination of fluid mechanics and electrochemistry studies is given by eq 30

$$\begin{aligned}\phi_l\rho_l\frac{\partial u_l}{\partial t} + \phi_l\rho_l u_l\cdot\nabla u_l &= -\nabla p + \nabla\cdot\left[\phi_l(\mu_l + \mu_T)\left(\nabla u_l + \nabla u_l^{\,T} - \frac{2}{3}(\nabla\cdot u_l)I\right)\right] \\ &\quad + \phi_l\rho_l g + F\end{aligned} \tag{30}$$

where ϕ is the phase volume fraction for gas and liquid, I is the identity matrix, μ_l (Pa s) is the dynamic viscosity, and μ_T (Pa s) is the turbulent viscosity. This equation considers negligible gas density, a slip model for gas velocity (the balance between viscous drag and pressure forces determines gas bubble motions), and the same pressure field for both phases. With the same assumptions, the continuity equation is given by (eq 31)

$$\frac{\partial}{\partial t}(\rho_l\phi_l + \rho_g\phi_g) + \nabla\cdot(\rho_l\phi_l u_l + \rho_g\phi_g u_g) = 0 \tag{31}$$

The gas phase transport equation is written as eq 32

$$\frac{\partial\rho_g\phi_g}{\partial t} + \nabla\cdot(\rho_g\phi_g u_g + \rho_g\phi_g u_g) = -m_{gl} \tag{32}$$

where m_{gl} (kg/m^3 s) is the mass transfer rate from gas to the liquid phase. Gas velocity is determined by eq 33.

$$u_g = u_l + u_{slip} \tag{33}$$

Momentum and continuity equations are simplified by assuming low gas concentration (ϕ_g = 0.01) in eqs 34 and 35.

$$\rho_l\frac{\partial u_l}{\partial t} + \rho_l u_l\cdot\nabla u_l = -\nabla p + \nabla\cdot[(\mu_l + \mu_T)(\nabla u_l + \nabla u_l^{\,T})] + \phi_l\rho_l g + F \tag{34}$$

$$\rho_l\nabla\cdot u_l = 0 \tag{35}$$

The cathode and anode gas mass flux is calculated by eq 36

$$N_{i,\mathrm{gas}} = \frac{i_{\mathrm{loc}}M_W}{4F} \tag{36}$$

where $N_{i,gas}$ (kg/m^2 s) is the gas mass flux, F is Faraday's constant, M_W (kg/mol) is the molar mass, and i_{loc} (A/m^2) is the local current density, which is calculated by eq 21. Pressure forces on a bubble are balanced by the drag force, and the pressure-drag balance is written as eq 37[47]

$$\phi_l\nabla p = -C_d\frac{3\rho_l}{4d_b}|u_{slip}|u_{slip} \tag{37}$$

where C_d is the drag coefficient and is modeled by the Hadamard−Rybczynski theorem for small spherical bubbles (for bubbles smaller than 2 mm), and d_b (m) is the bubble diameter. We included the bubble diameter and molar mass of ammonia[48] and oxygen[49] Table S4.

By solving eqs 1−37 using COMSOL Multiphysics, concentration gradients were modeled. Additional calculations were carried out to determine potential losses and pH distribution.

https://doi.org/10.1021/acs.iecr.3c04540
Ind. Eng. Chem. Res. 2024, 63, 9315−9328

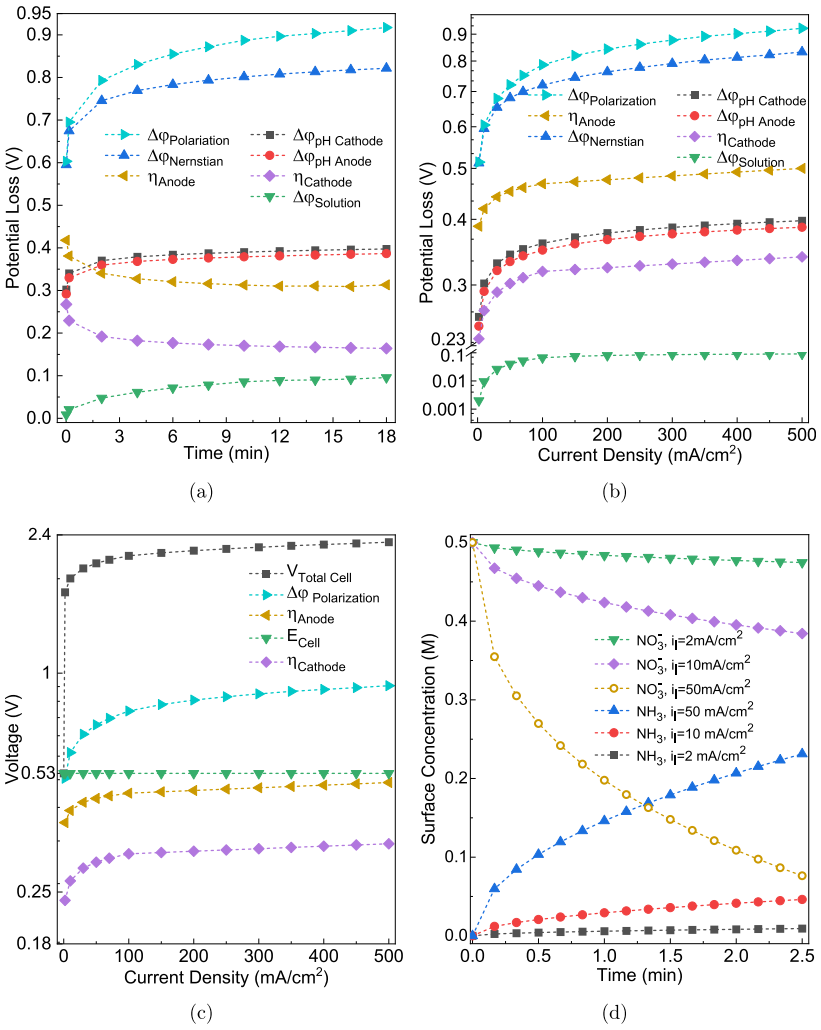

Figure 3. (a) Potential losses over time at i_l = 10 mA/cm^2 for the cell without membrane. Nernstian loss and solution loss (polarization loss) increase over time, while overpotentials decrease over time. The main part of the polarization loss is the cathode and anode pH loss (Nernstian Loss). (b) Potential loss for the current density range of 0−500 mA/cm^2 at BL = 300 μm. Both polarization loss and overpotentials increase when the current density increases (c) total cell voltage for the current density range of 0 to 500 mA/cm^2 at BL = 300 μm. Total cell voltage is equal to standard cell potential (0.53 V) at i_l = 0. The cell voltage only increases by around 26% from i_l = 10 to 500 mA/cm^2 (d) nitrate and ammonia surface concentrations (concentration near the cathode surface) over time at i_l = 2, 10, and 50 mA/cm^2 in the cell without a membrane. The surface concentration gradient decreases over time. The amount of decrease in nitrate concentration is not equal to the amount of increase in ammonia concentration, while they have the same stoichiometric coefficient. The reason is that nitrate diffuses to the anode surface due to electroneutrality. Cell properties are κ = 4.9 S/m, 0.5 M KNO_3, pH = 7.2, 100% selectivity toward ammonia production, $Ru_{15}CO_{75}$ is the catalyst for NO_3^-RR, and Ru_2O is the catalyst for OER.

RESULTS AND DISCUSSION

The polarization loss increases with increasing time and current density and eventually flattens out (Figure 3a−c). Polarization loss is calculated from modeled concentration profiles near the electrode surfaces. The major portion of the polarization loss corresponds to the Nernstian loss (∼37.5% for each electrode), which includes the Nernstian loss of reactants, cathode pH loss, and anode pH loss (eq 8, Figure 3a,b). Since pH gradients are more substantial than nitrate concentration gradients, the Nernstian loss associated with species is negligible compared to pH losses (Figures S4 and S5). The main portion of the solution loss is the Ohmic loss, and the diffusion losses of species are negligible (Figures S4 and S5). Ohmic loss is directly proportional to current density and inversely proportional to ionic conductivity, resulting in a nonlinear rise in Ohmic loss as current density increases (eq 5, Figure 3b). For instance, when the current density increases from 10 to 500 mA/cm^2, solution loss increases from 9.52 to 90.9 mV (nonlinear trend). The current density effect is more dominant than the ionic conductivity at lower current densities. However, the Ohmic loss starts to plateau at higher current densities and over time (Figure 3a,b). For Ohmic loss calculation, eq S9 was used with the initial value of κ = 4.9 S/m to model the conductivity along the cell and over time (Figure S6). Overpotentials are obtained by the intrinsic characteristics of the electrode toward each reaction. For example, when the current density increases from 2 to 10 mA/cm^2 and then to 50 mA/cm^2, ionic conductivity near the cathode surface (x = 0) increases from 5.502 to 7.750 S/m and 16.93 S/m at t = 180 s. To calculate the overpotential in the COMSOL electrolysis module, we require the kinetic parameters of the catalyst for each reaction. These parameters include the exchange current density (i_0) and anodic (α_a) and cathodic (α_c) transfer coefficients. We studied some of the recently developed

https://doi.org/10.1021/acs.iecr.3c04540
Ind. Eng. Chem. Res. 2024, 63, 9315−9328

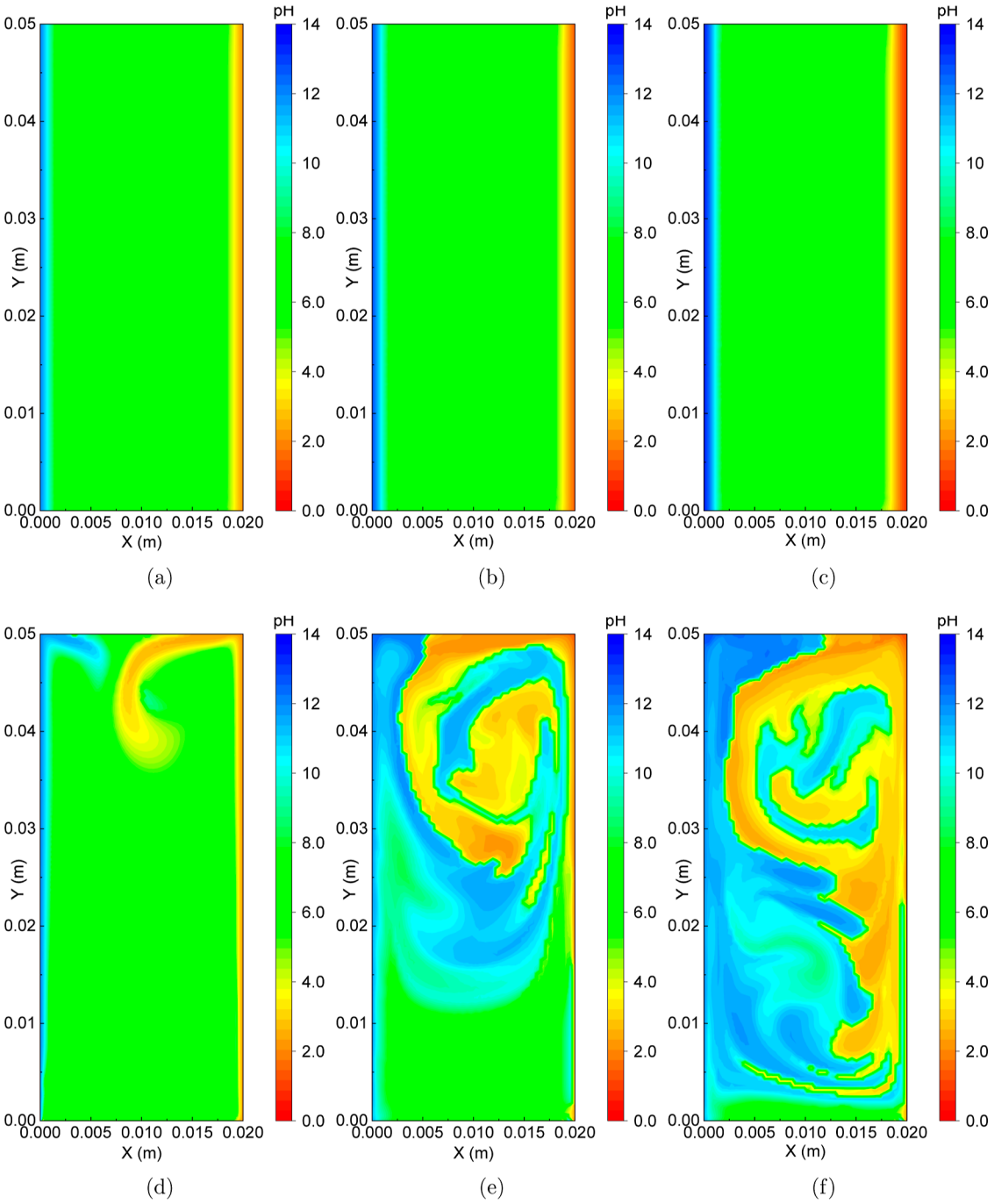

Figure 4. Comparison between the pH distribution of laminar and bubbly flow models along the cell at t = 10 s (a) pH distribution at i_l = 2 mA/cm^2 in the cell without the membrane and with laminar flow physics. (b) pH distribution at i_l = 10 mA/cm^2 in the cell without the membrane and with laminar flow physics. (c) pH distribution at i_l = 50 mA/cm^2 in the cell without the membrane and with laminar flow physics. (d) pH distribution at i_l = 2 mA/cm^2 in the cell without the membrane and with bubbly flow physics. (e) pH distribution at i_l = 10 mA/cm^2 in the cell without the membrane and with bubbly flow physics. (f) pH distribution at i_l = 50 mA/cm^2 in the cell without the membrane and with bubbly flow physics. The pH near electrode surfaces is lower in the bubbly flow model. The cell properties are κ = 4.9 S/m, 0.5 M KNO_3, pH = 7.2, 100% selectivity toward ammonia production, $Ru_{15}CO_{75}$ is the catalyst for NO_3^-RR, and Ru_2O is the catalyst for OER.

catalysts with favorable selectivity toward ammonia, including CO nanoarrays, Fe SAC, Cu/Cu_2O nanowires, Pd(111), and $Ru_{15}CO_{85}$. We acquired the kinetics data of each catalyst by using linear sweep voltammetry and Tafel plot data from the literature and applying eqs S16−S20 (Table S4, Figure S7).[13,16,43,50,51] We observed a similar trend in overpotential changes over time, regardless of catalyst characteristics (Figure S8). Among recent catalysts, Ruthenium cobalt alloys have shown a very low overpotential for the nitrate reduction reaction to ammonia. Thus, we selected $Ru_{15}Co_{85}$ as a material for the cathode catalyst.[43] eq S16 is used for calculating overpotential based on the kinetics behavior of the catalyst. We can also use eq 38 to calculate the overpotential(η)[52]

$$\eta = \phi_s - \phi_l - E_{eq} + \Delta\phi_{Nernstian} \quad (38)$$

https://doi.org/10.1021/acs.iecr.3c04540
Ind. Eng. Chem. Res. 2024, 63, 9315−9328

where ϕ_s (V) is the electrode potential, ϕ_l (V) is the electrolyte potential, and E_{eq} (V) is the equilibrium potential. Overpotential has a decreasing trend over time (Figure 3a). Based on modeling results, in eq 38, the difference between ϕ_s and ϕ_l remains approximately constant while $\Delta\phi_{Nernstian}$ increases in negative potentials. Thus, the overpotential decreases over time.

As the current density changes from 0 to 500 mA/cm^2, all polarization losses increase. This rise levels off over time and current density and almost flattens out for current densities higher than 80 mA/cm^2 (Figure 3b,c). For example, Nernstian loss increases from 751.3 to 923.2 mV when the current density rises from 100 to 500 mA/cm^2, which is only a ∼24% increase in loss for a 5-fold higher current density (Figure 3b). The total cell potential, which is used in energy efficiency calculations, is given by eq 39

$$V_{total} = E^0_{cell} + \eta_{anode} - \eta_{cathode} + \Delta\phi_{polarization} \quad (39)$$

$E_{NO_3^-RR}$ and E_{OER} are 0.7 and 1.23 V, respectively, resulting in a standard cell potential equal to 0.53 V ($E_{cell}{}^0 = E_{anode}{}^0 - E_{cathode}{}^0 = 0.53$ V). The total cell potential increases to ∼2.21 V at i_l = 100 mA/cm^2 and only increases ∼9.05% at i_l = 500 mA/cm^2 (2.29 V) (Figure 3c). Polarization losses and overpotentials at the cathode and anode surfaces increase the total cell potential to approximately 4-fold higher than that of the standard cell potential ($E_{cell}{}^0 = 0.53$ V) (Figure 3c). The total cell voltage (V_{total}) at current densities higher than 80 mA/cm^2 does not change drastically by current density; the increase in polarization loss will not be significant, and the energy efficiency drops by only 8.3% from 100 to 500 mA/cm^2 (Figure 3c). By increasing current density, cathodic and anodic reaction rates increase and, consequently, the concentrations of ammonia and oxygen near electrodes increase (Figures 3d and S9). For example, when the current density increases from i_l = 2 to 10 mA/cm^2, the ammonia concentration near the cathode surface (cathode surface at x = 0 m) increases from 0.00924 to 0.0462 M after 2.5 min, indicating the linear increase in surface concentrations with current density (Figure 3d). The same current-dependent behavior is observed for species in buffer solution ($H_2PO_4^-$ and HPO_4^{2-}), even though they are not directly involved in cathodic and anodic reactions (Figure S10). pH distribution near the electrode surface is current density dependent due to the production of hydroxide ions by the cathodic reaction and protons by the anodic reaction. As a result of the facile eight-electron transfer processes, these pH changes are substantial (around 5 units) over time (Figures 4, S11, eqs 1, 2, S1−S8, and S21−S23). With the fixed boundary layer thickness, as the current density increases, the absence of effective convection (stirring) leads to a depletion of nitrate concentration (approximately zero) near the cathode surface due to mass transfer limitations. This phenomenon significantly amplifies the concentration loss term of the Nernstian loss (eq 8), resulting in rapid rises in polarization loss and total cell voltage at current densities >250 mA/cm^2 (Figure S12).

pH gradients in the 2D laminar and bubbly flow models are presented by color maps (Figure 4). The boundary layer of the laminar flow model is simple to define and is similar for various current densities (Figure 4a−c). However, for bubbly flow, the fluid velocity changes the pH distribution and the shape of the boundary layer for various current densities (Figure 4d−f). In the bubbly flow model, electrolyte velocity increases the diffusion rate and changes the diffusion direction. This results in flow patterns different from those of the laminar flow (Figure 4). Flow velocity is governed by gas production, and its changes at higher local current densities are more pronounced as more gas is produced near electrode surfaces. The bubbly flow model has a more extended boundary of pH variation from the initial pH (7.2), and this boundary layer expansion increases at higher current densities (Figure 4). The pH change at the electrode surfaces is smaller in the bubbly flow compared to that of the laminar flow, resulting in a smaller Nernstian loss. These changes are about 4 units for bubbly flow and 5.5 units for laminar flow at the cathode surface for a current density of 50 mA/cm^2 (Figure 4).

The initial pH affects potential loss, especially for lower current densities (Figure S13). The Nernstian loss remains the major polarization loss for higher and lower pH values (Figure S13). When considering a higher or lower pH than 7.2, the increasing trend of polarization loss over time and the current density remain the same. By adding a 1 M buffer solution, polarization loss decreases by about 87% at t = 10 s in the current density range of 0 to 100 mA/cm^2 (Figure S14).

For alkaline cells, the hydroxide ion is consumed at the anode surface and produced at the cathode surface (eqs S5 and S6). Over time, the hydroxide ions are almost depleted near the anode surface. We assumed that after OH^- depletion, the former alkaline domain near the anode turns to an acidic domain because of the water equilibrium reaction. As a result, the anode reaction changes from eqs S5 to S2. For acidic cells, protons are consumed at the cathode surface and generated at the anode surface (eqs S2 and S3). Over time, protons are almost depleted at the cathode surface. We assumed that after H^+ depletion, the former acidic domain near the cathode turns to an alkaline domain due to the water equilibrium reaction. Therefore, the cathode reaction changes from eqs S6 to S3. As a result, for higher and lower pH values than neutral pH (7), a two-step study was performed at each current density. The solution for the first study was taken as an initial value for the second study. For moderate pH studies (pH = 4, 7.2, and 10), the time required for hydroxide ions and proton depletion is negligible. For instance, at pH = 13 and 10 and i_l = 10 mA/cm^2, the required time for hydroxide ions depletion at the anode surface is about 48.04 and 0.01 s. At pH = 1 and 4 and i_l = 10 mA/cm^2, the required time for proton depletion at the cathode surface is about 101 and 0.011 s. Our analysis shows that before hydroxide ion depletion at the anode surface (for pH > 7) and proton depletion at the cathode surface (for pH < 7), overpotentials are higher for both pH cases compared to neutral pH cases. Furthermore, in comparison with neutral pH, anode pH loss in the acidic electrolyte and cathode pH loss in the alkaline medium are lower than those of neutral-pH cases (Figure S13). Generally, until after a certain period of time (depending on current density), pH loss is smaller for extreme pH cases, but at higher current densities and longer time spans, the potential loss will be approximately equal for all pH cases when assuming 100% Faradaic efficiency (Figure S15). pH potential loss is calculated based on the pH difference between the bulk and the pH near the electrode surface. Therefore, for symmetrical changes from neutral pH (e.g., symmetrical changes from pH 7 are pH 1 and 13, which are both 6 units different from pH 7), we can assume the same pH difference between the boundary layer and the bulk. For initial pH = 1 and 13, over time, pH reaches around 13.5 and 0.5 near the cathode and anode surfaces. The absolute values for the

https://doi.org/10.1021/acs.iecr.3c04540
Ind. Eng. Chem. Res. 2024, 63, 9315−9328

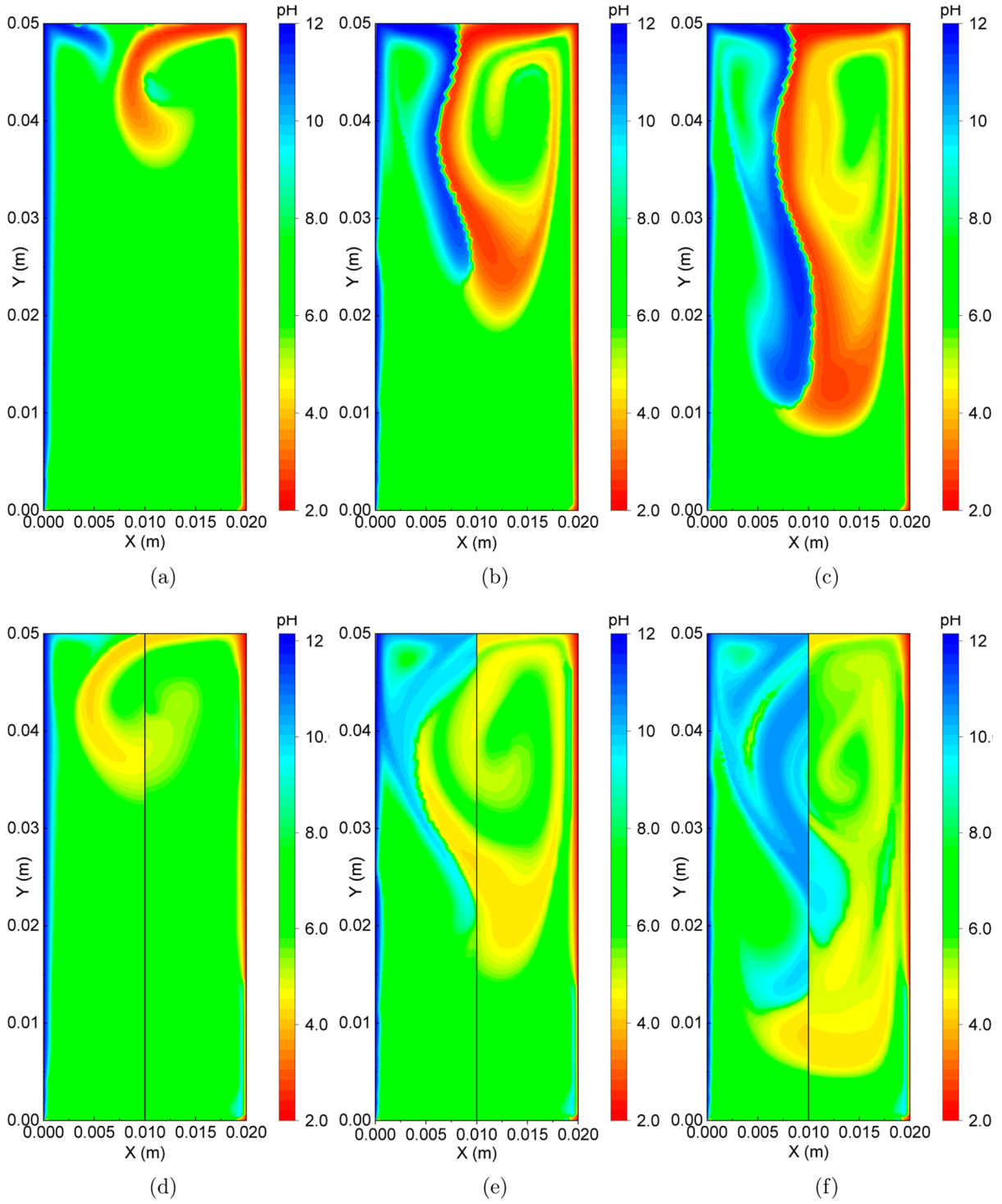

Figure 5. Comparison between pH distribution of the cells with and without membrane with bubbly flow physics along the cell and over time at i_l = 2 mA/cm^2 (a) pH distribution at t = 10 s, (b) at t = 20 s, and (c) at t = 30 s in the cell without membrane (d) pH distribution at t = 10 s, (e) at t = 20 s, and (f) at t = 30 s in the cell with membrane. In cells with a membrane, liquid velocity slows down because of the limited diffusion in the membrane. As a result, the acidic and alkaline regions are more spatially extended in the cell with a membrane. The cell properties are κ = 4.9 S/m, 0.5 M KNO_3, pH = 7.2, 100% selectivity toward ammonia production, $Ru_{15}CO_{75}$ is the catalyst for NO_3^-RR, and Ru_2O is the catalyst for OER.

cathodic and anodic pH differences with the bulk are 12.5 and 0.5 for pH = 1. These values are about the same for pH 13, except the anodic reaction experiences a much larger pH change (i.e., 12.5 units). Due to these equal differences in pH, the sum of the pH potential loss is similar for pH 1 and 13 (Figure S15).

The effect of pH on electrochemical nitrate reduction has been experimentally investigated in previous studies.[53] This study was carried out for an initial nitrate concentration of 0.0014 M. Experimental results showed that pH 7.5 was the optimal operating condition. We also selected near-neutral pH (7.2) as our main case study since the majority of wastewater sources have a pH near neutral (pH = 6−9).[54] The potential

https://doi.org/10.1021/acs.iecr.3c04540
Ind. Eng. Chem. Res. 2024, 63, 9315−9328

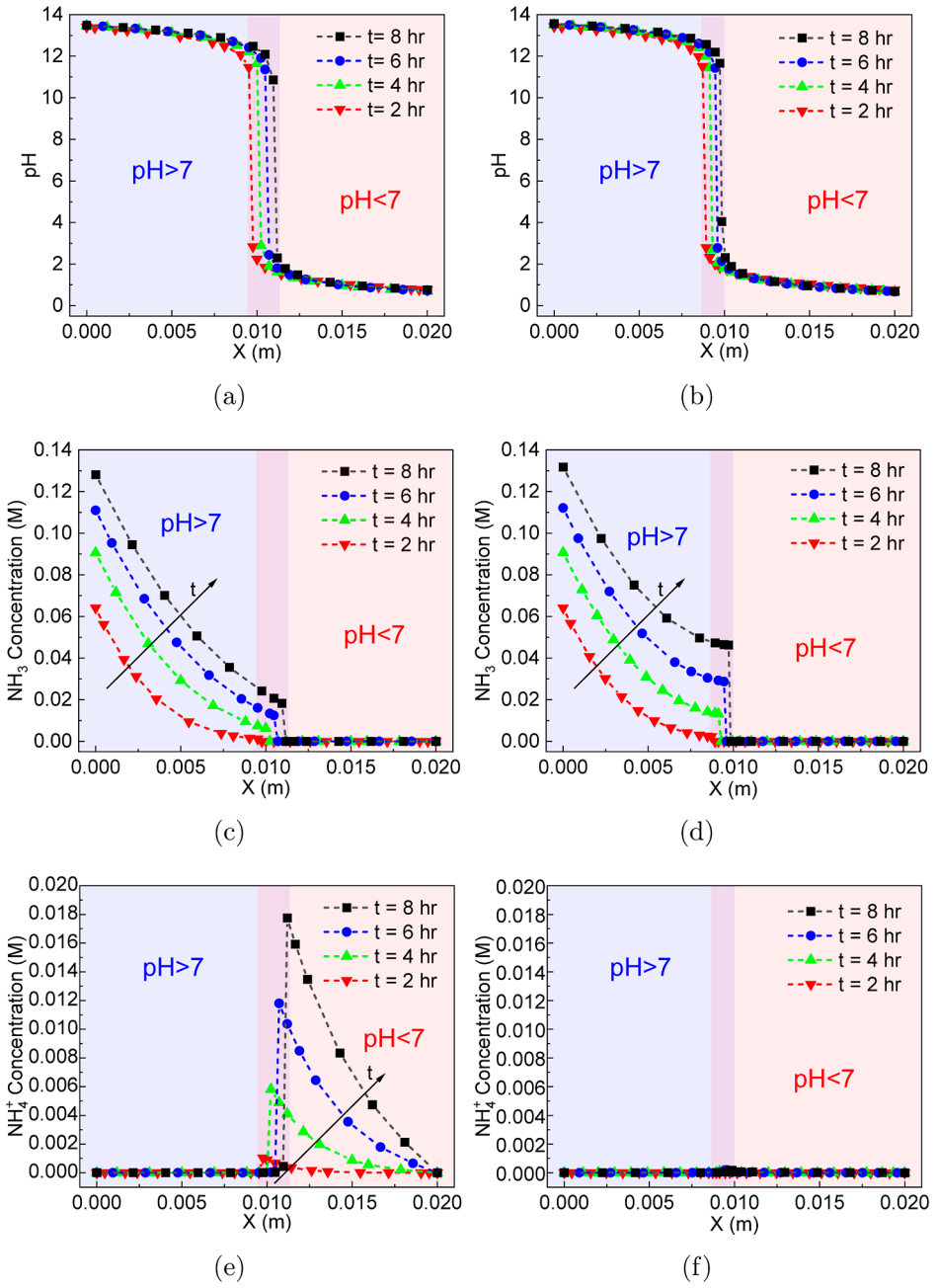

Figure 6. (a) pH distribution along the cell without the membrane at t = 2, 4, 6, and 8 h. By moving from the cathode surface at x = 0 to the anode surface at x = 0.02 m, alkaline media changes to acidic media (pH drops at 0.0095 < x < 0.011 m). (b) pH distribution along the cell with a membrane at t = 2, 4, 6, and 8 h. By moving from the cathode surface at x = 0 to the anode surface at x = 0.02 m, alkaline media changes to acidic media (pH drops at 0.0087 < x < 0.01 m), acidic media is more extended in the cell with membrane as hydroxide ions diffusion to the anode compartment is blocked by the membrane. (c) Ammonia concentration along the cell at t = 2, 4, 6, and 8 h and in the cell without membrane. Ammonia exists in alkaline media. (d) Ammonia concentration along the cell with a membrane at t = 2, 4, 6, and 8 h. Ammonia exists in alkaline media. Ammonia concentration is higher in a cell with a membrane than in a membrane-less system since ammonia does not diffuse into acidic media and convert to ammonium. (e) Ammonium concentration along the cell without a membrane at t = 2, 4, 6, and 8 h. Ammonia primarily exists in the ammonium form in the acidic media. (f) Ammonium concentration along the cell with a membrane at t = 2, 4, 6, and 8 h. Ammonium does not exist in this cell since the membrane prevents the ammonia from diffusing to the acidic compartment. The cell properties are κ = 4.9 S/m, 0.5 M KNO_3, pH = 7.2, i_l = 2 mA/cm^2, 100% selectivity toward ammonia production, $Ru_{15}CO_{75}$ is the catalyst for NO_3^-RR, and Ru_2O is the catalyst for OER.

losses for pH values of 4,7.2, and 10- are 7-fold higher than the polarization losses for pH values of 1 and 13 for current densities ranging from 0 to 20 mA/cm^2 at t = 10 s. However, for higher current densities, there is no significant difference between extreme pH cases (pH = 1 and 13) and moderate pH cases (pH = 4, 7.2, and 10) due to the rapid hydroxide ions and proton depletion at electrode surfaces (Figure S15). While a catalyst with the same performance and durability for both acidic and alkaline conditions has yet to be developed, here we aim to provide a comprehensive model that is applicable to a wide range of pH from 0 to 14. Utilizing flow cells can effectively minimize pH change near electrode surfaces. Within

https://doi.org/10.1021/acs.iecr.3c04540
Ind. Eng. Chem. Res. 2024, 63, 9315−9328

flow cells, wastewater is pumped in and out of the electrolyzer, enabling the replenishment of electrolytes near the cathode and the anode through continuous electrolyte recirculation. This dynamic flow operation near the electrode surfaces minimizes both pH changes and Nernstian loss.

A potential loss study for a specific amount of ammonia production can guide the prediction of system characteristics more accurately. The time required to produce certain moles of ammonia for different current densities increases linearly with the total moles of products near the cathode surface (Figure S16). Another approach is to look at the time required for removing a specific amount of nitrate (25, 50, and 100%) from the electrochemical cell. The required time for nitrate removal decreases exponentially by increasing the current density (Figure S17). Thus, at higher current densities (>70 mA/cm^2), the effect of increasing current density to decrease the required time for nitrate removal is not as significant as in the low current density regime (<50 mA/cm^2). We considered a specific amount of ammonia production (2 mmol) to understand whether the time decrease caused by increasing the current density has any effects on the potential loss. The outcome is independent of the amount of product since the yield linearly changes with the current density. The time required for different current densities to produce this amount of ammonia along the cell was determined by defining a stop condition for the ammonia molarity integration along the cell volume. The pH loss (the major polarization loss) for each current density was calculated by running the simulation for the specified time at each current density (Figure S18). To compare these losses at different current densities, the integration of potential losses over time was multiplied by the current density to calculate the energy loss of the system (eq 40 and Figure S19).

$$E_{\text{Loss}} = i_{\text{loc}} \int_0^t \Delta\phi(t)\, dt \tag{40}$$

where E_{Loss} (Wh) is the energy loss, and $\Delta\phi$ (V) is the potential loss. There is about a 10% change in energy loss from 10 to 100 mA/cm^2 (Figure S19). This indicates that operating the system at higher current densities will not drastically increase the potential loss but will remarkably accelerate the production rate and decrease the production time.

Protons have around a 2-fold higher diffusion coefficient ($D_{H+} = 9.31 \times 10^{-9}$ m/s) and subsequently 2-fold higher mobility than hydroxide ions ($D_{OH^-} = 5.27 \times 10^{-9}$ m/s) (Table S2 and eq 10). However, hydroxide ions have a higher stoichiometric coefficient ($\nu = 1.125$) than protons ($\nu = 1$) (eqs S7 and S8). In cells with laminar flow, the higher stoichiometric coefficient of hydroxide ions in smaller cells allows the alkaline region near the cathode surface to propagate through the anode half-cell, while in larger cells, the effect of the ions' mobility is more prominent, and the acidic region is more spatially extended (Figure S20a,b). The extension of alkaline media to the anodic half-cell neutralizes protons, preventing them from reaching the cathode surface (Figure S20b). When protons reach the cathode surface, they decrease the reaction quotient (Q in eq 7) and subsequently prevent potential loss ($E - E_0$) from increasing over time. By using CEM, protons can be transported from the anodic compartment to the cathodic compartment while the movement of hydroxide ions is blocked (Figure S20c,d). This changes the pH distribution along the cell and provides enough time for the protons generated at the anode to move to the cathodic compartment. The effect of the membrane is more significant in smaller cells (x = 6 mm) as it shrinks the alkaline media compared to the membrane-less system (Figure S20d).

In bubbly flow models with a 2 cm cell length, higher proton mobility plays a more significant role than the higher concentration of hydroxide ions over time, as observed with laminar flow models (Figure 5a−c). The effect of the membrane is more prominent in cells with bubbly flow fluid dynamics. The extent of acidic and alkaline regimes over time is more pronounced in the presence of the membrane in the bubbly flow models over time (Figure 5d−f). A more moderate pH gradient from the initial pH (7.2) is observed in bubbly flow models than that of the laminar flow, primarily due to the inclusion of liquid velocity in bubbly flow models (Figures 5d−f and S21a,c). Using a membrane results in lower diffusion coefficients for all species across the membrane. Therefore, species transport through the membrane occurs at rates slower than those of the electrolyte. This is also interpreted as lower liquid velocity across the membrane, resulting in different concentration and velocity profiles in comparison with the cell without a membrane. The magnitude of liquid velocity is greater near the electrode surfaces and gas outlets and is lower near the membrane in both anodic and cathodic compartments, as shown by velocity profiles at t = 30 s (Figure S21). This results in a higher gas collection rate in cells with a membrane (Figure S21).

The hydrogen evolution reaction (HER) is a prominent competing reaction at the cathode surface. While high faradaic efficiencies (70−100%) could be achieved during electrochemical NO_3^-RR to ammonia, we examine HER effects for faradaic efficiencies of 70 and 85%. Despite no change in potential loss due to continuous proton consumption at the cathode surface, variations in the velocity and pH profiles occur within the bubbly flow model. This discrepancy originates from the lighter and faster diffusion of hydrogen bubbles compared with ammonia bubbles. In cases with lower ammonia faradaic efficiencies, hydrogen exits the cell rapidly, leading to the formation of a smaller region characterized by alkaline pH and lower velocities (Figures S22 and S23).

The membrane affects the ammonium and ammonia distribution along the cell (Figure 6). Ammonia solubility in water depends on the temperature and the pH (Figures S24, S25 and eqs S24−S33). At the anode surface, protons are produced or hydroxide ions are consumed, causing the anodic compartment to become acidic. In addition, protons are consumed or hydroxide ions are produced at the cathode surface, making the cathodic compartment alkaline over time. Moving from the cathode surface (x = 0) to the anode surface (x = 0.02), pH changes from alkaline (around 13) to acidic (around 1) along the cell (Figure 6a). In the presence of the membrane, less extended alkaline media are observed over time (Figure 6b). Regardless of using a membrane, no noticeable ammonia is present in the anodic half-cell, primarily due to the dominance of acidic media (Figure 6c,d). When the membrane is used, the ammonia concentration is greater at the cathodic compartment over time due to the blockage of ammonia diffusion to the anodic half cell (Figure 6d). As a result, ammonia does not reach the acidic medium near the anode surface and remains in its initial form (NH_3). In the absence of the membrane, due to the pH distribution in the cell, the diffused ammonia into the acidic region with a pH

https://doi.org/10.1021/acs.iecr.3c04540
Ind. Eng. Chem. Res. 2024, 63, 9315−9328

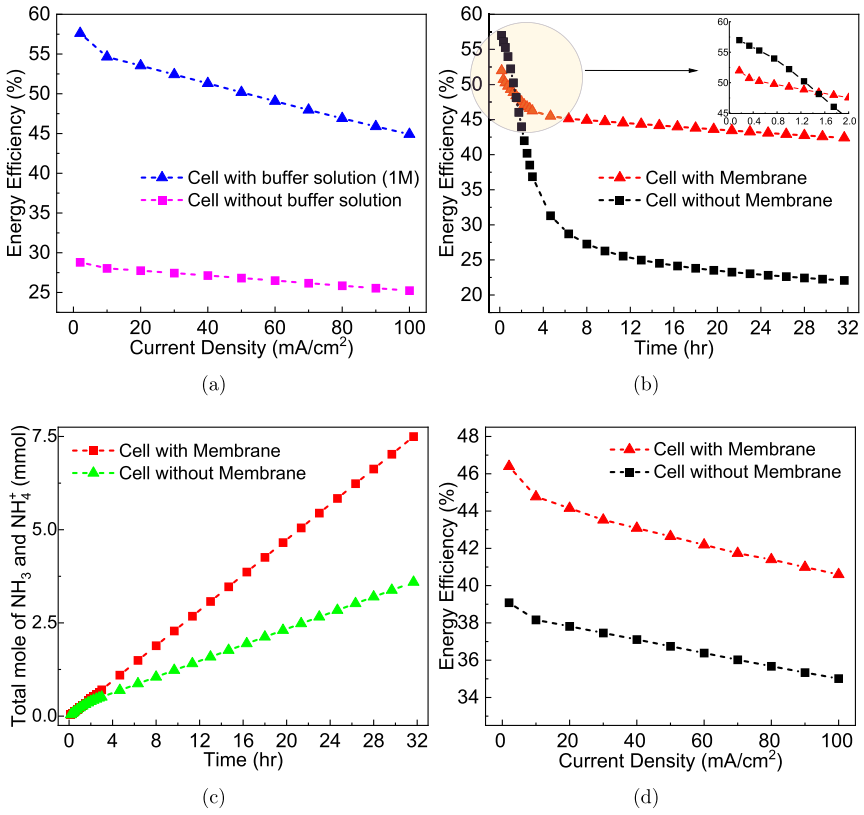

Figure 7. Energy efficiency comparison over time and the current density range of 0 to 100 mA/cm^2 (a) energy efficiency comparison over the current density range of 0 to 100 mA/cm^2 at t = 10 s with and without buffer solution (buffer concentration = 1 M) (b) Energy efficiency comparison over time for 100% nitrate removal at i_l = 2 mA/cm^2 for the cell with 1 M buffer solution with and without membrane. (c) Total moles of ammonia and ammonium over time for 100% nitrate removal at i_l = 2 mA/cm^2 for the cell with 1 M buffer solution with and without membrane. (d) Energy efficiency comparison for cells with a 1 M buffer solution with and without the membrane at t = 2.5 h. Cell properties are κ = 4.9 S/m, 0.5 M KNO_3, pH = 7.2, 100% selectivity toward ammonia production, $Ru_{15}CO_{75}$ is the catalyst for NO_3^-RR, and Ru_2O is the catalyst for OER.

lower than ammonia pK_a (9.251 at T = 25 °C) over time reacts with water and produces ammonium cations and hydroxide ions (Figure 6e and eq S23). In this region, all ammonia (NH_3) is converted to ammonium (NH_4^+) (Figure 6e). In the presence of the membrane, no ammonia could diffuse, and therefore, no such conversion of ammonia to ammonium is noticed (Figure 6f).

We calculated the energy efficiency of the cell by using eqs 41 and S34

$$\eta_{EE\%} = \frac{E^0_{cell}}{V_{total}} \times \eta_{FE\%} \tag{41}$$

where $\eta_{PEE\%}$ is the energy efficiency, and $\eta_{FE\%}$ is the Faradaic efficiency. The Faradaic efficiency of the electrocatalytic process is calculated by eq 42

$$FE = \frac{n_p nF}{Q} = \frac{n_p nF}{It} \tag{42}$$

where I (A/cm^2) is the current density, n_p (mol/(cm^2 h)) is the total number of moles of the product, Q (C) is the total charge passed through the system, F (C/mol) is the Faraday's constant, and n is the number of electrons required to produce 1 mol of the desired species. As potential loss increases over time and current density, the energy efficiency decreases, according to eq 41. In the absence of the buffer solution, pH potential loss increases, resulting in an energy efficiency of ~27% at i = 10 mA/cm^2 and t = 10 s. The energy efficiency increases to ~55% by adding buffer species and minimizing pH loss near electrode surfaces (Figure 7a). As the current density increases, the effect of buffer solution on the reduction of pH loss decreases. Thus, the difference between energy efficiency in electrochemical cells with and without buffer solution drops from 30% at i = 2 mA/cm^2 to 20% at i = 100 mA/cm^2 (Figure 7a). The membrane alters the concentration profiles along the cell and necessitates potential loss calculations near the membrane surfaces in both anodic and cathodic half-cells. In cells with proton-conductive membranes (i.e., CEM), the hydroxide concentration changes at the membrane boundary layer in the cathodic compartment. This results in a rise in ohmic loss and cathode pH loss, which are the main portions of the potential loss increase (Figure S26). The total change in potential loss after using a membrane is about 100 mV. This rise in potential loss results in lower energy efficiency by ~5% initially (Figure 7b). However, as ammonia diffuses to the anode surface in a membrane-less system, it is oxidized to nitrogen gas over time, resulting in the loss of the product and lower energy efficiencies over time compared to those of the membrane-based system (Figures 7b, S27, eqs S35 and S36). In addition, for ammonia oxidation, a larger cell voltage is required to drive anodic reactions, leading to a decrease in energy efficiency (eqs 41 and S34). The most effective way to prevent ammonium oxidation is to use a membrane that blocks ammonia and ammonium diffusion to the anodic compartment. By using a membrane, the total moles of ammonia in the solution are 3-fold greater than those of a membrane-less

https://doi.org/10.1021/acs.iecr.3c04540
Ind. Eng. Chem. Res. 2024, 63, 9315−9328

system after 32 h (Figure 7c). Thus, the membrane offsets the initial efficiency drop by preventing ammonia diffusion and, subsequently, its oxidation at the anode over time (Figure 7b). After 32 h and 100% nitrate removal at i = 2 mA/cm^2, the energy efficiency of the cell without membrane reaches ∼22% due to the ammonia oxidation at the anode surface, while the energy efficiency of the cell with membrane only reduces to ∼42% (Figure 7b). The decrease in energy efficiency at higher current densities is due to the increase in cell voltage as the current density increases from 0 to 100 mA/cm^2 (Figure 7d). At t = 2.5 h, energy efficiency reduces by ∼6% for the cell with membrane (46.5 to 40.5%) and ∼4.5% for the cell without membrane (39 to 34.5%) in the current density range of 0 to 100 mA/cm^2 (Figure 7d).

CONCLUSIONS

We computationally studied the origin of potential losses and pH distributions in electrochemical NO_3^-RR to ammonia. We found that bubbly flow physics represents a more accurate pH distribution near electrode surfaces and along the cell, mimicking the turbulent flow induced by the generation of gases near electrodes. The effect of the membrane on the electrolysis cell is more noticeable in the bubbly flow model as it alters liquid velocity and, eventually, pH distribution. The most significant portion of the potential loss is the anode and cathode pH losses, which account for ∼34% of the total cell voltage. The use of buffer solutions can help minimize these types of losses. Although the use of a membrane increases potential loss due to the increase in iR loss initially, in long-term operation, it prevents ammonia oxidation at the anode surface, which diffuses from the cathode. This results in higher energy efficiencies in contrast to the membrane-less system. This work offers a framework to investigate various operational design parameters, including cell length, current density, pH, conductivity, buffer solution, and the choice of membrane that must be optimized to develop a more efficient electrochemical cell that optimizes production time, yield, and energy efficiency.

ASSOCIATED CONTENT

Supporting Information

The Supporting Information is available free of charge at https://pubs.acs.org/doi/10.1021/acs.iecr.3c04540.

1D cell configurations, Nernstian and diffusion losses of species, kinetics of electrodes, polarization loss for cell with membrane, for cell with pH = 13, cell with buffer solution, nitrate removal dependency on time and current density, ammonia solubility analysis, and detailed analysis of spatial and temporal conductivity and concentrations (PDF)

AUTHOR INFORMATION

Corresponding Author

Mohammadreza Nazemi − *Department of Mechanical Engineering, Colorado State University, Fort Collins, Colorado 80523, United States; School of Materials Science and Engineering, Colorado State University, Fort Collins, Colorado 80524, United States;* orcid.org/0000-0002-1735-9277; Email: Reza.Nazemi@colostate.edu

Author

Maryam Ahmadi − *Department of Mechanical Engineering, Colorado State University, Fort Collins, Colorado 80523, United States*

Complete contact information is available at: https://pubs.acs.org/10.1021/acs.iecr.3c04540

Author Contributions

M.A. and M.N. conceived the idea. M.A. conducted all the simulations, analyzed the data, and wrote the manuscript. M.N. provided direction, edited the manuscript, and supervised the study.

Notes

The authors declare no competing financial interest.

ACKNOWLEDGMENTS

This material is based upon work supported by the Colorado Office of Economic Development and International Trade (OEDIT) under grant no. 5302887. The authors are grateful to Hydrofuel Inc. for partially supporting this work. This material is based on work supported by the National Science Foundation under grant no. 1904351. COMSOL technical staff are acknowledged for their help and support throughout this work.

REFERENCES

(1) Lehnert, N.; Dong, H. T.; Harland, J. B.; Hunt, A. P.; White, C. J. Reversing nitrogen fixation. *Nat. Rev. Chem* **2018**, *2*, 278−289.

(2) Smil, V. *Enriching the Earth: Fritz Haber, Carl Bosch, and the Transformation of World Food Production*; The MIT Press: Cambridge, MA, 2004.

(3) Nazemi, M.; El-Sayed, M. A. Managing the nitrogen cycle via plasmonic (photo) electrocatalysis: toward circular economy. *Acc. Chem. Res.* **2021**, *54*, 4294−4304.

(4) Nazemi, M.; Panikkanvalappil, S. R.; El-Sayed, M. A. Enhancing the rate of electrochemical nitrogen reduction reaction for ammonia synthesis under ambient conditions using hollow gold nanocages. *Nano Energy* **2018**, *49*, 316−323.

(5) Nolan, B. T.; Ruddy, B. C.; Hitt, K. J.; Helsel, D. R. Risk of Nitrate in groundwaters of the United States a national perspective. *Environ. Sci. Technol.* **1997**, *31*, 2229−2236.

(6) Environmental Protection Agency. *U. S. E. P. A. National Primarily Drinking Water Regulations*, 2006.

(7) Kumar, M.; Chakraborty, S. Chemical denitrification of water by zero-valent magnesium powder. *J. Hazard. Mater.* **2006**, *135*, 112−121.

(8) Nazemi, M.; El-Sayed, M. A. *Photo-electrochemical Ammonia Synthesis: Nanocatalyst Discovery, Reactor Design, and Advanced Spectroscopy*; CRC Press: Boca Raton, FL, 2021.

(9) Ma, Y.; Bae, J. W.; Kim, S.-H.; Jovičević-Klug, M.; Li, K.; Vogel, D.; Ponge, D.; Rohwerder, M.; Gault, B.; Raabe, D. Reducing Iron Oxide with Ammonia: A Sustainable Path to Green Steel. *Advanced Science* **2023**, *10*, No. e2300111.

(10) Valera-Medina, A.; Amer-Hatem, F.; Azad, A. K.; Dedoussi, I. C.; de Joannon, M.; Fernandes, R. X.; Glarborg, P.; Hashemi, H.; He, X.; Mashruk, S.; et al. Review on Ammonia as a Potential Fuel: From Synthesis to Economics. *Energy Fuels* **2021**, *35*, 6964−7029.

(11) Nazemi, M.; Ou, P.; Alabbady, A.; Soule, L.; Liu, A.; Song, J.; Sulchek, T. A.; Liu, M.; El-Sayed, M. A. Electrosynthesis of ammonia using porous bimetallic Pd−Ag nanocatalysts in liquid-and gas-phase systems. *ACS Catal.* **2020**, *10*, 10197−10206.

(12) Bulk Chemicals *Ammonia Market Size, Share & Trends Analysis Report by Product Form (Aqueous, Anhydrous), by Application (Fertilizers, Refrigerants, Pharmaceuticals, Textile), by Region, and Segment Forecasts*, 2023−2030. Grand View Research Report ID: GVR-2−68038−207−5.

(13) Wu, Z.-Y.; Karamad, M.; Yong, X.; Huang, Q.; Cullen, D. A.; Zhu, P.; Xia, C.; Xiao, Q.; Shakouri, M.; Chen, F.-Y.; et al. Electrochemical ammonia synthesis via nitrate reduction on Fe single atom catalyst. *Nat. Commun.* **2021**, *12*, 2870.
(14) Pérez-Gallent, E.; Figueiredo, M. C.; Katsounaros, I.; Koper, M. T. Electrocatalytic reduction of Nitrate on Copper single crystals in acidic and alkaline solutions. *Electrochim. Acta* **2017**, *227*, 77−84.
(15) Wang, Y.; Xu, A.; Wang, Z.; Huang, L.; Li, J.; Li, F.; Wicks, J.; Luo, M.; Nam, D. H.; Tan, C. S.; et al. Enhanced Nitrate-to-Ammonia Activity on Copper-Nickel Alloys via Tuning of Intermediate Adsorption. *J. Am. Chem. Soc.* **2020**, *142*, 5702−5708.
(16) Wang, Y.; Zhou, W.; Jia, R.; Yu, Y.; Zhang, B. Unveiling the activity origin of a copper-based electrocatalyst for selective nitrate reduction to ammonia. *Angew. Chem., Int. Ed.* **2020**, *59*, 5350−5354.
(17) Fan, X.; Zhao, D.; Deng, Z.; Zhang, L.; Li, J.; Li, Z.; Sun, S.; Luo, Y.; Zheng, D.; Wang, Y.; et al. Constructing Co@TiO_2 nanoarray heterostructure with Schottky contact for selective electrocatalytic nitrate reduction to ammonia. *Small* **2023**, *19*, No. e2208036.
(18) Fan, X.; Ma, C.; Zhao, D.; Deng, Z.; Zhang, L.; Wang, Y.; Luo, Y.; Zheng, D.; Li, T.; Zhang, J.; Sun, S.; Lu, Q.; Sun, X. Unveiling selective nitrate reduction to ammonia with Co_3O_4 nanosheets/TiO_2 nanobelt heterostructure catalyst. *J. Colloid Interface Sci.* **2023**, *630*, 714−720.
(19) Fan, X.; He, X.; Ji, X.; Zhang, L.; Li, J.; Hu, L.; Li, X.; Sun, S.; Zheng, D.; Luo, Y.; Wang, Y.; Xie, L.; Liu, Q.; Ying, B.; Sun, X. High-efficiency electrosynthesis of ammonia with selective reduction of nitrite over an Ag nanoparticle-decorated TiO_2 nanoribbon array. *Inorg. Chem. Front.* **2023**, *10*, 1431−1435.
(20) He, X.; Li, Z.; Yao, J.; Dong, K.; Li, X.; Hu, L.; Sun, S.; Cai, Z.; Zheng, D.; Luo, Y.; Ying, B.; Hamdy, M. S.; Xie, L.; Liu, Q.; Sun, X. High-efficiency electrocatalytic nitrite reduction toward ammonia synthesis on CoP@TiO_2 nanoribbon array. *iScience* **2023**, *26*, 107100.
(21) Rameshan, R.; Tiwari, A.; Kanungo, S.; Roy, S. Rags to Riches: Meliorating the Electrocatalytic Reduction of Nitrate to Ammonia over Cu-Based Nanoalloys. *Inorg. Chem.* **2023**, *62*, 9934−9944.
(22) Fan, X.; Liu, C.; Li, Z.; Cai, Z.; Ouyang, L.; Li, Z.; He, X.; Luo, Y.; Zheng, D.; Sun, S.; et al. others Pd-Doped Co_3O_4 Nanoarray for Efficient Eight-Electron Nitrate Electrocatalytic Reduction to Ammonia Synthesis. *Small* **2023**, *19*, 2303424.
(23) Ouyang, L.; Liang, J.; Luo, Y.; Zheng, D.; Sun, S.; Liu, Q.; Hamdy, M. S.; Sun, X.; Ying, B. Recent advances in electrocatalytic ammonia synthesis. *Chin. J. Catal.* **2023**, *50*, 6−44.
(24) Chen, F.-Y.; Wu, Z.-Y.; Gupta, S.; Rivera, D. J.; Lambeets, S. V.; Pecaut, S.; Kim, J. Y. T.; Zhu, P.; Finfrock, Y. Z.; Meira, D. M.; et al. Efficient conversion of low-concentration nitrate sources into ammonia on a Ru-dispersed Cu nanowire electrocatalyst. *Nat. Nanotechnol.* **2022**, *17*, 759−767.
(25) Liu, M. J.; Guo, J.; Hoffman, A. S.; Stenlid, J. H.; Tang, M. T.; Corson, E. R.; Stone, K. H.; Abild-Pedersen, F.; Bare, S. R.; Tarpeh, W. A. Catalytic performance and near-surface X-ray characterization of titanium hydride electrodes for the electrochemical nitrate reduction reaction. *J. Am. Chem. Soc.* **2022**, *144*, 5739−5744.
(26) Wu, X.; Nazemi, M.; Gupta, S.; Chismar, A.; Hong, K.; Jacobs, H.; Zhang, W.; Rigby, K.; Hedtke, T.; Wang, Q.; Stavitski, E.; Wong, M. S.; Muhich, C.; Kim, J.-H. Contrasting Capability of Single Atom Palladium for Thermocatalytic versus Electrocatalytic Nitrate Reduction Reaction. *ACS Catal.* **2023**, *13*, 6804−6812.
(27) Andersson, M.; Paradis, H.; Yuan, J.; Sundén, B. Three dimensional modeling of an solid oxide fuel cell coupling charge transfer phenomena with transport processes and heat generation. *Electrochim. Acta* **2013**, *109*, 881−893.
(28) Rossi, M.; Wallmersperger, T.; Neukamm, S.; Padberg-Gehle, K. Modeling and Simulation of Electrochemical Cells under Applied Voltage. *Electrochim. Acta* **2017**, *258*, 241−254.
(29) Wu, J.; Zheng, W.; Chen, Y. Factors affecting the cathode/electrolyte interfacial pH change during water reduction: A simulation study. *Int. J. Hydrogen Energy* **2022**, *47*, 18597−18605.
(30) Kuhn, A.; Chan, C. pH changes at near-electrode surfaces. *J. Appl. Electrochem.* **1983**, *13*, 189−207.
(31) Obata, K.; Van De Krol, R.; Schwarze, M.; Schomäcker, R.; Abdi, F. F. In situ observation of pH change during water splitting in neutral pH conditions: impact of natural convection driven by buoyancy effects. *Energy Environ. Sci.* **2020**, *13*, 5104−5116.
(32) Singh, M. R.; Clark, E. L.; Bell, A. T. Effects of electrolyte, catalyst, and membrane composition and operating conditions on the performance of solar-driven electrochemical reduction of carbon dioxide. *Phys. Chem. Chem. Phys.* **2015**, *17*, 18924−18936.
(33) Singh, M. R.; Papadantonakis, K.; Xiang, C.; Lewis, N. S. An electrochemical engineering assessment of the operational conditions and constraints for solar-driven water-splitting systems at near-neutral pH. *Energy Environ. Sci.* **2015**, *8*, 2760−2767.
(34) Kani, N. C.; Prajapati, A.; Singh, M. R. Sustainable Routes for Photo-Electrochemical Synthesis of Ammonia Using Various Nitrogen Precursors. *ACS ES&T Eng.* **2022**, *2*, 1080−1087.
(35) Weast, R. C.; Lide, D.; Astle, M.; Beyer, W. *CRC Handbook of Chemistry and Physics*; CRC Press: Boca Raton, FL, 1989.
(36) Appelo, C. Solute transport solved with the Nernst-Planck equation for concrete pores with 'free' water and a double layer. *Cem. Concr. Res.* **2017**, *101*, 102−113.
(37) Dwight, E. *American Institute of Physics Handbook*; McGraw Hill: New York, NY, 1972.
(38) Sharma, A. K.; Ahmed, K.; Birgersson, E. Nernst voltage losses in planar fuel cells caused by changes in chemical composition: Effects of operating parameters. *Ionics* **2018**, *24*, 2047−2054.
(39) Bard, A. J.; Faulkner, L. R.; White, H. S. *Electrochemical Methods: Fundamentals and Applications*; John Wiley: Hoboken, NJ, 2022.
(40) Wu, J.; Zheng, W.; Chen, Y. Factors affecting the cathode/electrolyte interfacial pH change during water reduction: A simulation study. *Int. J. Hydrogen Energy* **2022**, *47*, 18597−18605.
(41) Hao, S.; Liu, M.; Pan, J.; Liu, X.; Tan, X.; Xu, N.; He, Y.; Lei, L.; Zhang, X. Dopants fixation of Ruthenium for boosting acidic oxygen evolution stability and activity. *Nat. Commun.* **2020**, *11*, 5368.
(42) Ryden, W.; Lawson, A.; Sartain, C. C. Electrical Transport Properties of IrO_2 and RuO_2. *Phys. Rev. B* **1970**, *1*, 1494−1500.
(43) Han, S.; Li, H.; Yu, Y.; Zhang, B.; Yang, R.; Yu, Y.; Zhang, B. Ultralow overpotential nitrate reduction to ammonia via a three-step relay mechanism. *Nat. Catal.* **2023**, *6*, 1−13.
(44) Daniels, L.; Sahu, S.; Sanders, K. J.; Goward, G. R.; Foster, J. M.; Protas, B. Learning Optimal Forms of Constitutive Relations Characterizing Ion Intercalation from Data in Mathematical Models of Lithium-Ion Batteries. *J. Phys. Chem. C* **2023**, *127*, 17508−17523.
(45) Cai, J.; Wei, Y.; Cao, A.; Huang, J.; Jiang, Z.; Lu, S.; Zang, S.-Q. Electrocatalytic nitrate-to-ammonia conversion with ∼100% Faradaic efficiency via single-atom alloying. *Appl. Catal., B* **2022**, *316*, 121683.
(46) Chen, J.-Q.; Ye, X.-X.; Zhou, D.; Chen, Y.-X. Roles of Copper in Nitrate Reduction at Copper-Modified Ru/C Catalysts. *J. Phys. Chem. C* **2023**, *127*, 2918−2928.
(47) Schwarz, M.; Turner, W. Applicability of the standard k-ϵ turbulence model to gas-stirred baths. *Appl. Math. Model.* **1988**, *12*, 273−279.
(48) Kobayashi, T.; Fujioka, S.; Tanaka, S.; Terasaka, K. Microbubble generation with rapid dissolution of ammonia (NH_3)-hydrogen (H_2) mixed gas fed from a nozzle into water. *Chem. Eng. Sci.* **2022**, *248*, 117155.
(49) Hamad, F.; Pun, K.; Alessio, B.; Najim, S.; Ganesan, P.; Hughes, D. Experimental measurements on the microbubble characteristics and dissolved oxygen (DO) in water using single and twin-Venturi type microbubble generators. *Chem. Eng. Sci.* **2023**, *280*, 118994.
(50) Deng, X.; Yang, Y.; Wang, L.; Fu, X.-Z.; Luo, J.-L. Metallic Co nanoarray catalyzes selective NH_3 production from electrochemical nitrate reduction at current densities exceeding 2 Acm^{-2}. *Adv. Sci.* **2021**, *8*, 2004523.
(51) Han, Y.; Zhang, X.; Cai, W.; Zhao, H.; Zhang, Y.; Sun, Y.; Hu, Z.; Li, S.; Lai, J.; Wang, L. Facet-controlled palladium nanocrystalline

https://doi.org/10.1021/acs.iecr.3c04540
Ind. Eng. Chem. Res. 2024, 63, 9315−9328

for enhanced nitrate reduction towards ammonia. *J. Colloid Interface Sci.* **2021**, *600*, 620−628.
(52) Girault, H. H. *Analytical and Physical Electrochemistry*; EPFL press: New York, NY, 2004.
(53) Nguyen, T. N. P.; Chen, P. C.; Huang, C. Nitrate removal and extracellular polymeric substances of autohydrogenotrophic bacteria under various pH and hydrogen flow rates. *J. Environ. Sci.* **2018**, *63*, 50−57.
(54) Meese, A. F.; Kim, D. J.; Wu, X.; Le, L.; Napier, C.; Hernandez, M. T.; Laroco, N.; Linden, K. G.; Cox, J.; Kurup, P.; et al. Opportunities and Challenges for Industrial Water Treatment and Reuse. *ACS ES&T Eng.* **2021**, *2*, 465−488.

https://doi.org/10.1021/acs.iecr.3c04540
Ind. Eng. Chem. Res. 2024, 63, 9315−9328